ACS APPLIED MATERIALS & INTERFACES

www.acsami.org

Research Article

Ag−Bi_2O_3-Nanostructured Composite Electrodes toward Catalyzing Oxygen Evolution Reaction: Exploring Oxygen Evolution Reaction Kinetics in Composites from Doping to Establishing a Heterojunction

Que Thi Nguyen, Umesh T. Nakate,* Balaji G. Ghule, Soojin Park, Jeongsik Choi, Jong Hyun Park, Jae Ryang Park, Ji-Hyun Jang, Dong-Won Kim, and Sungjune Park*

Cite This: *ACS Appl. Mater. Interfaces* 2025, 17, 12307−12316

Read Online

ACCESS | Metrics & More | Article Recommendations | Supporting Information

ABSTRACT: Electrochemical water splitting involving two-half chemical cell reactions is a promising approach to generate hydrogen and oxygen. Although this method is sustainable, the sluggish kinetics of the oxygen evolution reaction (OER) occurring at the anode due to a high overpotential is an issue to be addressed. Recently, various chemical and structural engineering approaches have been explored to improve the efficiency of the OER by reducing the overpotential. Among them, incorporating noble metals into the electrodes by doping or creating heterojunctions is an appealing approach to develop efficient OER electrocatalysts. Based on this principle, herein, we synthesized a bismuth-oxide (Bi_2O_3) electrocatalyst incorporated with silver nanoparticles (Ag NPs) by a facile one-step hydrothermal method to take advantage of the high conductivity of Ag NPs and the low band gap along with fast redox reaction of Bi_2O_3. With the Ag^+ concentration in the hydrothermal precursor solution, the thickness of hydrothermally formed Bi_2O_3 nanoplates decreases, resulting in the increased electrochemical surface area (ECSA) from 71 to 300 cm^2. The optimal electrode, heterojunction-formed Ag−Bi_2O_3 (denoted H-$Ag_{1.00}$-Bi_2O_3), exhibits the lowest overpotential of 260 mV for the OER at a current density of 10 mA cm^{-2} with an excellent durability of 77.5% after stability tests for 240 h due to the number of active sites produced by Ag doping (manifesting defects), and heterojunction established between Ag nanoparticles and Bi_2O_3 nanoplates. The approach explored in this work could be further utilized to produce other effective electrocatalysts for accelerating OER performances.

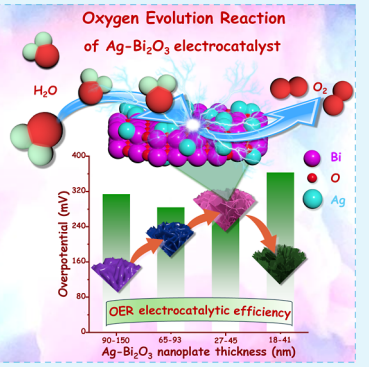

KEYWORDS: *water splitting, oxygen evolution reaction, electrocatalysts, Ag−Bi_2O_3-nanostructured composites, heterojunction and doping*

INTRODUCTION

Electrocatalytic water splitting (EWS) is a promising approach to generating hydrogen at the cathode [hydrogen evolution reaction (HER)] and oxygen at the anode [oxygen evolution reaction (OER)] surfaces by applying an external potential.[1] Although, HER has gained substantial attention as a sustainable way to generate hydrogen environmentally,[2,3] the sluggish kinetics of the OER due to the high overpotential (≥1.23 V) inevitably retards HER simultaneously.[4] Therefore, various studies have recently focused on developing electrocatalysts to accelerate OER activity by overcoming the high overpotential.[5]

Among various OER electrocatalysts, RuO_2 and IrO_2 are recognized as excellent candidates, but they have limitations in terms of cost and scarcity.[6] Therefore, numerous alternative electrocatalysts, such as transition-metal alloys, noble metals, and post-transition metals, have been developed to replace them.[7−9] Transition metals are resistant to corrosion and can easily be functionalized by incorporating with heterogeneous metals to form composite materials; however, their intrinsically limited conductivity hinders electron transfer during electrolysis, thereby limiting EWS performances. Post-transition metals are also promising due to their unique electronic-, optoelectronic-, and catalytic properties;[10−12] however, the oxide layer on their surface may reduce conductivity, resulting in insufficient electrical properties for electrochemical applications. To address this issue, incorporating a small amount of highly conductive agents, such as noble metals, into nanostructured post-transition metals is considered a compelling strategy to synthesize effective electrocatalysts due to multiple oxidation states and facile formation of uniform 3D nanostructures of post-transition metals.[13] Recently, as an example of noble-metal-decorated post-transition-metal oxide nanostructures, Bi_2O_3 decorated with silver (Ag), gold (Au),

Received: December 17, 2024
Revised: February 11, 2025
Accepted: February 12, 2025
Published: February 17, 2025

https://doi.org/10.1021/acsami.4c22156
ACS Appl. Mater. Interfaces 2025, 17, 12307−12316

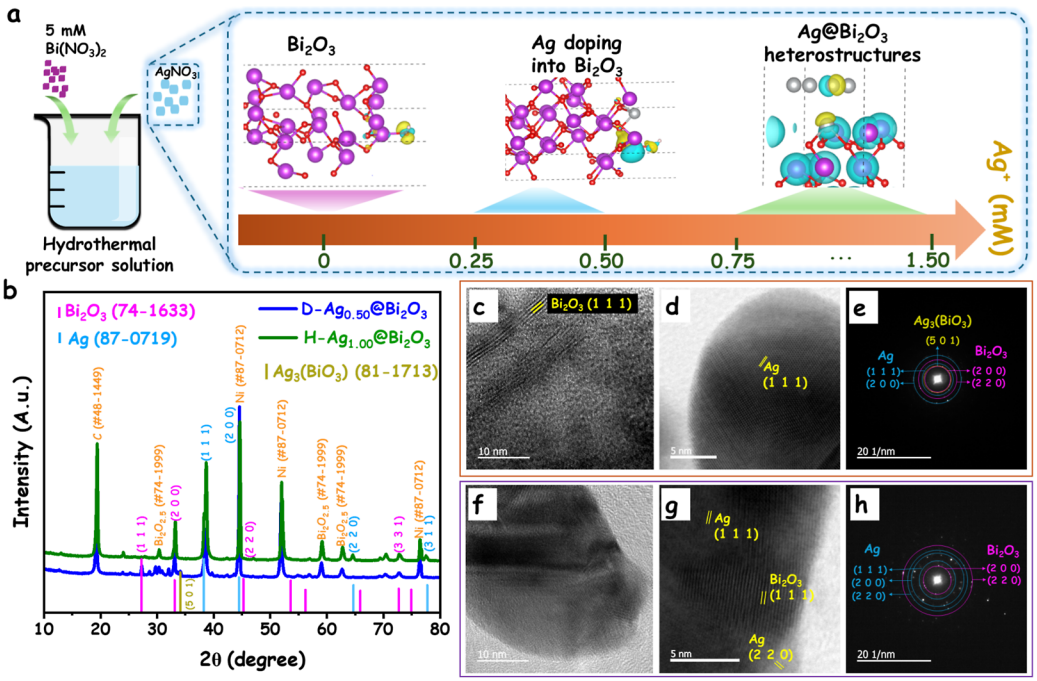

Figure 1. (a) Preparation of the hydrothermal precursor solution, (b) XRD patterns of D-$Ag_{0.50}$@Bi_2O_3 and H-$Ag_{1.00}$@Bi_2O_3, (c,d,f,g) HR-TEM images, and (e,h) SAED patterns of (c–e) D-$Ag_{0.50}$@Bi_2O_3 and (f–h) H-$Ag_{1.00}$@Bi_2O_3.

and platinum (Pt) have demonstrated their superior catalytic properties for various electrocatalytic applications.[14,15] In particular, Ag-incorporated Bi_2O_3 (Ag–Bi_2O_3) have demonstrated their unique synergistic effects[16,17] by taking advantage of the low band gap (2.6–3.9 eV), facile formation of various nanostructures of Bi_2O_3,[18] as well as the relatively high metallic conductivity of Ag.[19]

In principle, topographies and electronic properties are key parameters for optimization in OER electrocatalysts.[20] Doping introduces trace or small amounts of a dopant (≤10 wt % of the host material) and generates impurities in the host material's structure; consequently, the electronic structure can be tuned without changing the host material's topography.[21] In contrast, establishing a heterojunction may induce complementary properties, i.e., both diverse topographies and built-in electric fields can be generated and influence the kinetics of OER.[22] Based on this underlying principle, we designed various forms of Ag–Bi_2O_3 electrocatalysts: (i) Bi_2O_3 nanoplates (no Ag), (ii) Ag-doped Bi_2O_3 nanoplates, and (iii) Ag–Bi_2O_3 with heterojunctions, by identifying the various ratios of the materials. The morphological and electrical differences, as well as the OER performances affected by them, were distinguished and explored by various characterization methods. Moreover, density functional theory (DFT) was simulated for clarifying the atomic structure of Ag–Bi_2O_3 in doping, heterojunction, and the kinetic energy during OER on the surface of these samples. According to the results, the thickness of the Bi_2O_3 nanoplates decreased with an increase in Ag^+ concentrations, resulting in larger electrode/electrolyte interfaces that may accelerate the redox reaction. Among the various electrodes, the sample named H-$Ag_{1.00}$@Bi_2O_3 (Ag–Bi_2O_3 with a heterojunction synthesized by using an Ag^+ concentration of 1.0 mM) exhibits the highest OER performance, with a low overpotential of 260 mV at 10 mA cm^{-2}, a low Tafel slope of 141 mV dec^{-1}, and a large electrochemical surface area (ECSA) of 230 cm^{-2}. The stability of the sample was tested for up to 240 h, and a real-state full-cell test using double AAA batteries as an external potential supplier was performed to explore its stability for 72 h under a 1.0 M KOH electrolyte solution. The H-$Ag_{1.00}$@Bi_2O_3 electrocatalyst demonstrated its durability by maintaining a stability of 91.1% compared to its initial value after 100 h of testing. This strategy to synthesize composite electrodes by doping and establishing heterojunctions via incorporating heterogeneous elements could be further extended to develop other effective combinations of electrodes for wide applications.

RESULTS AND DISCUSSION

Structural and Morphological Characterizations. As shown in the schematic in Figure 1a, a hydrothermal synthesis was employed to produce Ag–Bi_2O_3 electrocatalysts. To understand the morphological evolution of Ag–Bi_2O_3 as a function of concentration in Ag^+ in the hydrothermal precursor solution, a range of Ag^+ concentrations from 0 to 1.5 mM was utilized. Depending on the Ag^+ concentrations, two growth mechanisms were identified: (i) Ag doping into Bi_2O_3 (samples denoted D-$Ag_{0.25}$@Bi_2O_3 and D-$Ag_{0.50}$@Bi_2O_3) at low concentrations of Ag^+ (from 0.25 to 0.50 mM) and (ii) establishment of a heterojunction between Ag and Bi_2O_3 (samples denoted H-$Ag_{0.75}$@Bi_2O_3 to H-$Ag_{1.50}$@Bi_2O_3) at high concentrations of Ag^+ (from 0.75 to 1.50 mM). Table S1 details the synthetic conditions for all of the electrocatalysts.

The distinctions between Ag doping into Bi_2O_3 and establishing a heterojunction with Ag–Bi_2O_3 were confirmed through morphological and electrocatalytic characterizations. X-ray diffraction (XRD) analyses of D-$Ag_{0.50}$@Bi_2O_3 and H-$Ag_{1.00}$@Bi_2O_3 (Figure 1b), along with pristine Bi_2O_3 and Ag (Figure S1), revealed the face-centered cubic crystal structure of δ-Bi_2O_3 (JCPDS-74-1633) with characteristic peaks at 2θ angles of 31.6°, 45.2°, 65.9°, and 72.8° corresponding to (1 1 1), (2 2 0), (0 0 2), and (1 1 0) planes, respectively, indicating highly crystalline structures.[23] The presence of Ag metal was

https://doi.org/10.1021/acsami.4c22156
ACS Appl. Mater. Interfaces 2025, 17, 12307–12316

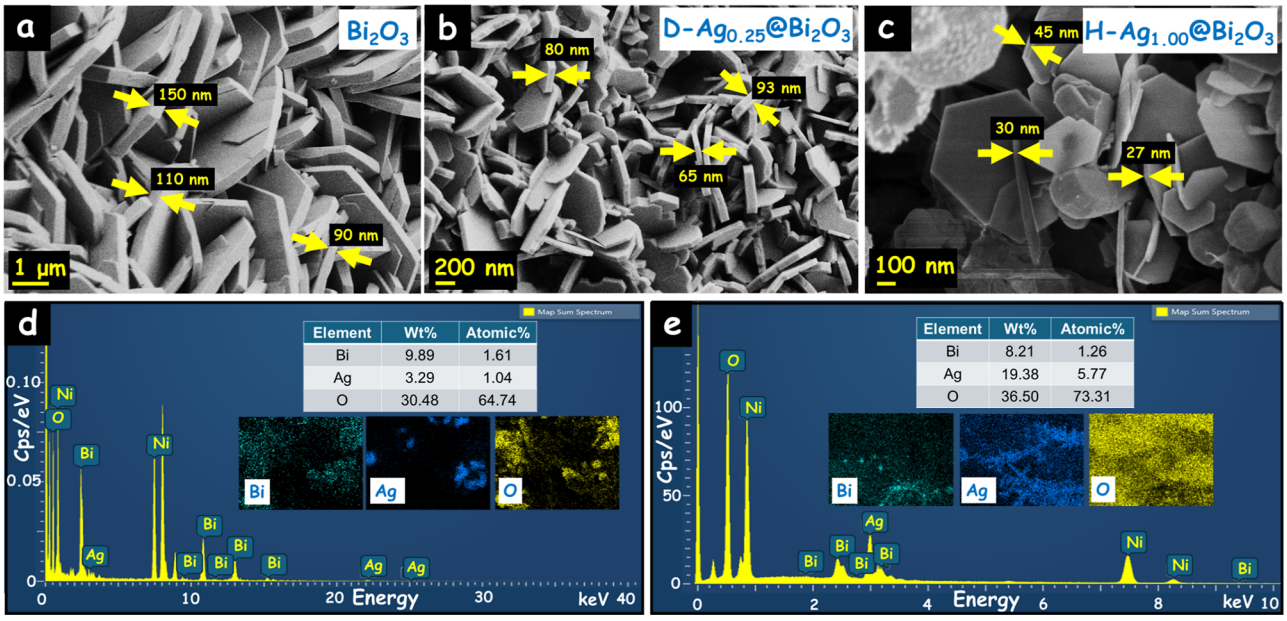

Figure 2. (a–c) FE-SEM images of (a) Bi_2O_3, (b) D-$Ag_{0.50}$@Bi_2O_3, (c) H-$Ag_{1.00}$@Bi_2O_3, and (d,e) EDS mapping of (d) D-$Ag_{0.50}$@Bi_2O_3 and (e) H-$Ag_{1.00}$@Bi_2O_3.

confirmed by reflections at 38.26° (1 1 1), 44.48° (2 0 0), 64.71° (2 2 0), and 77.74° (3 1 1) from JCPDS-87-0719.[24] Notably, a peak at 33.13° (5 0 1) indicated the presence of $Ag_3(BiO_3)$ in D-$Ag_{0.50}$@Bi_2O_3 according to JCPDS-81-1713, confirming successful Ag doping into Bi_2O_3.[25] We note that the existence of C (JCPDS-48-1449) and Ni (JCPDS-87-0712) originated from a carbon tape and a nickel foam substrate, as described in Figure S2. On the other hand, $Bi_2O_{2.5}$ peaks confirmed by JCPDS-74-1999 were formed probably due to the bismuth ions reduced by the high temperature and pressure applied during the hydrothermal synthesis.[26] The crystallite sizes of the materials were characterized using transmission electron microscopy (TEM) and HR-TEM, as shown in Figure 1c,d,f,g, for D-$Ag_{0.50}$@Bi_2O_3 and H-$Ag_{1.00}$@Bi_2O_3, respectively. The average interplanar distances were estimated via fast Fourier transforms, with Bi_2O_3 (1 1 1) at 0.32 nm and Ag (1 1 1) at 0.23 nm.

Moreover, selected area electron diffraction (SAED) was employed to analyze the diffraction patterns. In principle, the diameter of each ring corresponds to the interplanar distance of identical crystalline phases observed in the XRD patterns. The primary distinction between D-$Ag_{0.50}$@Bi_2O_3 and H-$Ag_{1.00}$@Bi_2O_3 lies in the concentration of Ag^+ in the hydrothermal precursor solution. Therefore, in D-$Ag_{0.50}$@Bi_2O_3 (Figure 1e), bold rings correlate with high-intensity XRD peaks of Ag (1 1 1) (2 0 0) and $Ag_3(BiO_3)$ (5 0 1). In contrast, a faint ring associated with the XRD peak of Ag (2 2 0) is observed in the SAED pattern of H-$Ag_{1.00}$@Bi_2O_3 (Figure 1h), indicating a higher Ag content within the lattice structures of H-$Ag_{1.00}$@Bi_2O_3 (Ag (1 1 1) and Ag (2 2 0)) compared to D-$Ag_{0.50}$@Bi_2O_3 (Ag (1 1 1)); the higher ratio of lattice structures of H-$Ag_{1.00}$@Bi_2O_3 may result in higher OER performances than that of D-$Ag_{0.50}$@Bi_2O_3. The calculation SAED results shown in Figure S3 provide approximate "*d*" values based on information from JCPDS-74-1633 (Bi_2O), JCPDS-87-0719 (Ag), and JCPDS-81-1713 ($Ag_3(BiO_3)$).

As depicted in FE-SEM images (Figure 2), the electrocatalysts exhibit nanoplate-like structures with an average length of approximately 500 nm. The Bi_2O_3 nanoplates show a thickness of approximately 100 nm (Figure 2a), which decreases with increasing Ag^+ concentration due to the Ag impurities retarding the recrystallization of Bi_2O_3 in the composite. As shown in Figure 2b,c, D-$Ag_{0.50}$@Bi_2O_3 and H-$Ag_{1.00}$@Bi_2O_3 display thinner nanoplates of 65–93 and 27–45 nm, respectively. The FE-SEM image of H-$Ag_{1.50}$@Bi_2O_3 obtained from the highest Ag^+ concentration (1.50 mM) in the hydrothermal precursor solution shows the thinnest nanoplate thickness (18–41 nm), highlighting the influence of the heterogeneous element (Ag) on the growth inhibition of Bi_2O_3 nanostructures (Figure S4). Thinner nanoplates inherently provide larger surface areas with numerous topographical pores, enhancing the electrode–electrolyte interfaces crucial for promoting redox reactions during the OER performance. Consequently, the Ag–Bi_2O_3 electrodes exhibit stronger potential than pure Bi_2O_3 for accelerating OER performance.

To characterize the distribution of elements on the thin layers of the electrodes, EDS mapping of D-$Ag_{0.50}$@Bi_2O_3 and H-$Ag_{1.00}$@Bi_2O_3 is analyzed, as shown in Figure 2d,e. The presence of elements Ni (from the nickel substrate), Bi, and O (from Bi_2O_3), as well as Ag (from doping and heterojunctions), confirmed the successful formation of Ag–Bi_2O_3 on the nickel substrate by hydrothermal synthesis. As shown in the energy count per second (Cps) graphs, D-$Ag_{0.50}$@Bi_2O_3 exhibits higher energy but lower Cps (energy range: 0–30 kV, Cps: 0–0.2 eV) compared to H-$Ag_{1.00}$@Bi_2O_3 (energy range: 0–10 kV, Cps: 0–150 eV), indicating a lower density of Ag element on the surface of D-$Ag_{0.50}$@Bi_2O_3, which may require higher energy to obtain lower response Cps than H-$Ag_{1.00}$@Bi_2O_3. As Ag incorporates more into Bi_2O_3, it may inhibit the formation of Bi_2O_3, resulting in thinner nanoplates of Bi_2O_3, as supported by FE-SEM images and mapping extracted from HR-TEM images (Figure S5).

The full-scan XPS spectra of D-$Ag_{0.50}$@Bi_2O_3 and H-$Ag_{1.00}$@Bi_2O_3 across a broad range of binding energy (BE) from 0 to 600 eV are shown in Figures 3a and S6a. For comparison, the

https://doi.org/10.1021/acsami.4c22156
ACS Appl. Mater. Interfaces 2025, 17, 12307–12316

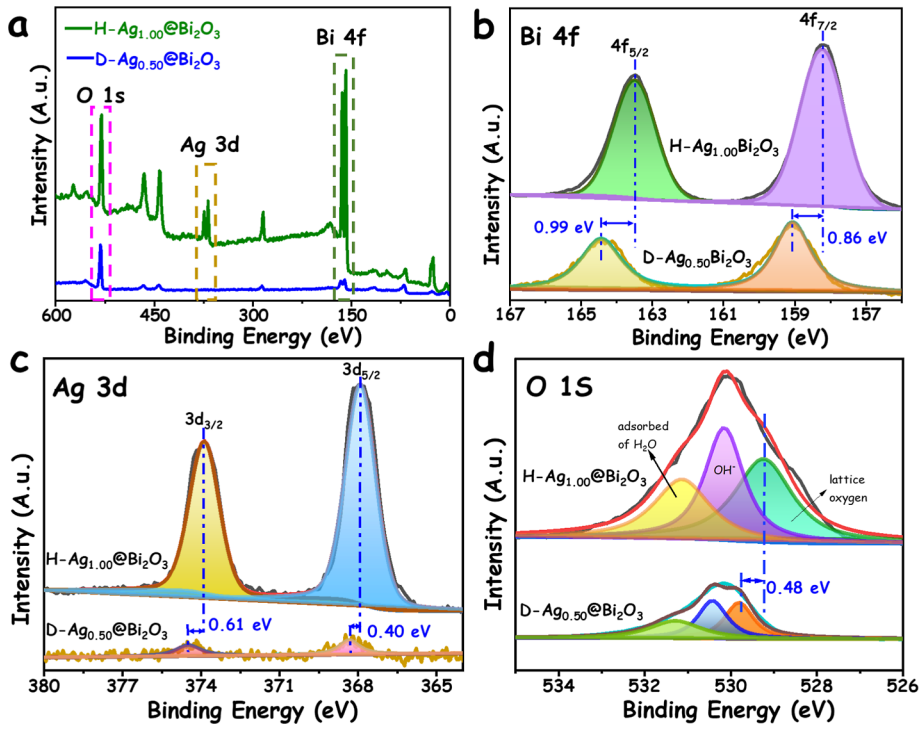

Figure 3. (a) Full-scan XPS spectrum and (b–d) XPS profiles of (b) Bi 4f, (c) Ag 3d, and (d) O 1s for D-$Ag_{0.50}@Bi_2O_3$ and H-$Ag_{1.00}@Bi_2O_3$.

XPS spectrum of pure Bi_2O_3 is presented in Figure S6. The high-resolution spectra of Bi 4f and Ag 3d show doublets at BEs around 150–170 and 360–380 eV, respectively. The O 1s spectrum appears as a sharp peak at approximately 500 eV BE. Due to the low concentration of Ag 3d in D-$Ag_{0.50}@Bi_2O_3$, the intensity of the Ag 3d peaks is too small to identify. The atomic ratio (Bi 4f/Ag 3d) extracted from the full-width at half-maximum in XPS was compared to the molar ratio (Bi^{3+}/Ag^{+}) of the hydrothermal precursor solution, as shown in Table S2. The discrepancy between XPS results and the molar ratio (Bi^{3+}/Ag^{+}) of the hydrothermal precursor solution is probably due to the limitation of the surface characterization methods such as XPS and EDS mapping used to scan up to the microscale depth of the sample. However, inductively coupled plasma optical emission spectroscopy (ICP-OES) was used to analyze the content and the ratio of Bi and Ag in the composites by measuring the emission spectra of elements in a plasma. By acid-treatment of the samples at 200 °C for 16 h, the composite of $Ag@Bi_2O_3$ was dissolved and subsequently formed Bi^{3+} and Ag^{+} in the solution. As shown in Table S3, the element ratios of Bi/Ag in D-$Ag_{0.50}@Bi_2O_3$ and H-$Ag_{1.00}@Bi_2O_3$ are 10.71:1.00 and 3.16:1.00, respectively; while the molar ratio of Bi^{3+}/Ag^{+} in the hydrothermal precursor solutions for D-$Ag_{0.50}@Bi_2O_3$ and H-$Ag_{1.00}@Bi_2O_3$ is approximately 10.00:1.00 and 5.00:1.00, respectively.

The XPS profiles of Bi 4f are shown in Figures 3b and S6b; the BE values of pure Bi_2O_3 at the peak positions of $4f_{5/2}$ and $4f_{7/2}$ are 164.5 and 159.2 eV, respectively.[27] However, in the binary Ag–Bi_2O_3 samples, the peak positions shift toward a negative direction, including D-$Ag_{0.50}@Bi_2O_3$ (164.4 and 159.0 eV, respectively) and H-$Ag_{1.00}@Bi_2O_3$ (163.4 and 158.2 eV, respectively). Note there are two factors presumably affecting the shifting of BE values of Bi 4f in XPS results: (1) the lower electronegativity of Ag compared to Bi (1.93 and 2.02, respectively) and (2) the increased atomic ratios of Ag (4.73% in H-$Ag_{1.00}@Bi_2O_3$ and 0.27% in D-$Ag_{0.50}@Bi_2O_3$). Thus, the paired electrons in the Ag–Bi bond prefer to move toward Bi due to the higher electronegativity of Bi,[28] causing a greater number of electrons surrounding Bi as a function of the Ag ratio in the electrode. Clearly, with the same Bi nuclear energy, the increased electron density surrounding it induces a lower BE between the single electron and the Bi nucleus; therefore, the energy required to separate electrons in Bi 4f from the Bi atom decreases, resulting in the negatively shifted BE values of the electrodes with increasing Ag ratios (H-$Ag_{1.00}@Bi_2O_3$ < D-$Ag_{0.50}@Bi_2O_3$ < Bi_2O_3).[29]

In Figure 3c, the high-resolution Ag 3d spectrum is fitted with two distinguished peaks. The BE values of Ag $3d_{3/2}$ and $Ag_{5/2}$ were located at 374.0, 368.1 eV (for H-$Ag_{1.00}@Bi_2O_3$), and 374.6. The BE value of 368.5 eV (for D-$Ag_{0.50}@Bi_2O_3$) indicated the presence of metallic Ag (Ag^0) in the electrocatalyst.[30] While the peaks located at 529.3 (H-$Ag_{1.00}@Bi_2O_3$) and 529.8 eV (D-$Ag_{0.50}@Bi_2O_3$) correspond to lattice oxygen (O^{2-}) in the Bi–O bond,[31] the higher BE components can be ascribed to the hydroxide (OH^-) and adsorption of H_2O from the air and humidity[32] (Figures 3d and S6c).

Electrocatalytic Properties. The electrocatalytic properties of the electrodes for the OER application were studied in a 1.0 M KOH electrolyte under ambient conditions. The results of linear sweep voltammetry (LSV), overpotential (η), Tafel slopes, Nyquist plots, chronopotentiometry, full-cell device tests, and DFT calculations are discussed. The LSV was conducted at a low scan rate of 2 mV s^{-1} to explore the electron-transfer kinetics in redox reactions. Figure 4a,b presents the LSV curves of the electrocatalysts at current densities of 200 and 70 mA cm^{-2}, respectively. The overpotential and Tafel slope of Bi_2O_3, D-$Ag_{0.25}@Bi_2O_3$, H-$Ag_{1.00}@Bi_2O_3$, and NF are shown in Figure 4c,d, respectively. The polarization curve of NF exhibits an authenticated oxidative peak at 1.37 V vs reversible hydrogen electrode,

https://doi.org/10.1021/acsami.4c22156
ACS Appl. Mater. Interfaces 2025, 17, 12307–12316

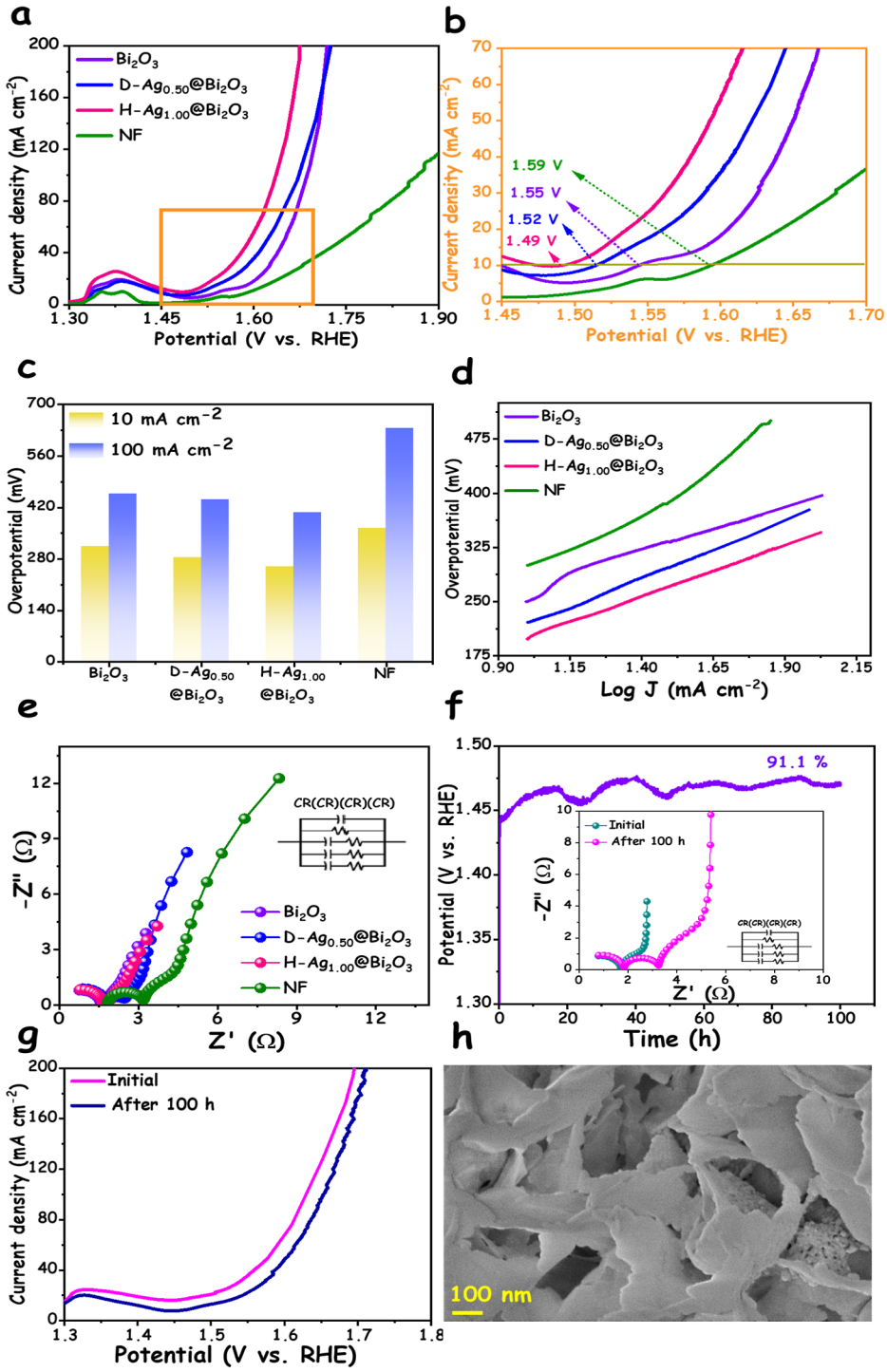

Figure 4. (a) LSV curves with IR_s correction, (b) LSV curves at low current density, (c) overpotential (η) at current densities of 10 and 100 mA cm^{-2}, (d) corresponding Tafel plots, (e) Nyquist plots of Bi_2O_3, D-$Ag_{0.50}$@Bi_2O_3, H-$Ag_{1.00}$@Bi_2O_3, and NF, and (f) chronopotentiometry of H-$Ag_{1.00}$@Bi_2O_3 at a current density of 10 mA cm^{-2} during electrochemical testing for 100 h; the inset shows the Nyquist plots, (g) LSV curves before and after the stability test for 100 h and (h) FE-SEM image of H-$Ag_{1.00}$@Bi_2O_3 after the stability test for 100 h.

verifying the oxidation reaction of Ni species in all samples due to the NF substrate.[33] For the OER application, NF demonstrates a poor electrocatalytic efficiency with overpotentials of 363 and 635 mV at 10 and 100 mA cm^{-2}, respectively, a high Tafel slope of 244 mV dec^{-1}, and an electrode resistance (R_s) of 1.7 Ω and was extracted from the Nyquist plot. Thus, the enhanced OER performance is primarily attributed to the Ag−Bi_2O_3 electrocatalysts.

Compared to NF, the improved OER performance is observed for pure Bi_2O_3 nanoplates deposited on the NF substrate, presumably due to the low band gap of bismuth-based materials and the highly flexible conversion of Bi^{2+}/Bi^{3+}. The overpotential is reduced to 314 mV at 10 mA cm^{-2}, while at a high current density of 100 mA cm^{-2}, the overpotential is effectively improved to 457 mV compared to that of bare NF. The Tafel slope and R_s values were also reduced to 150 mV

https://doi.org/10.1021/acsami.4c22156
ACS Appl. Mater. Interfaces 2025, 17, 12307−12316

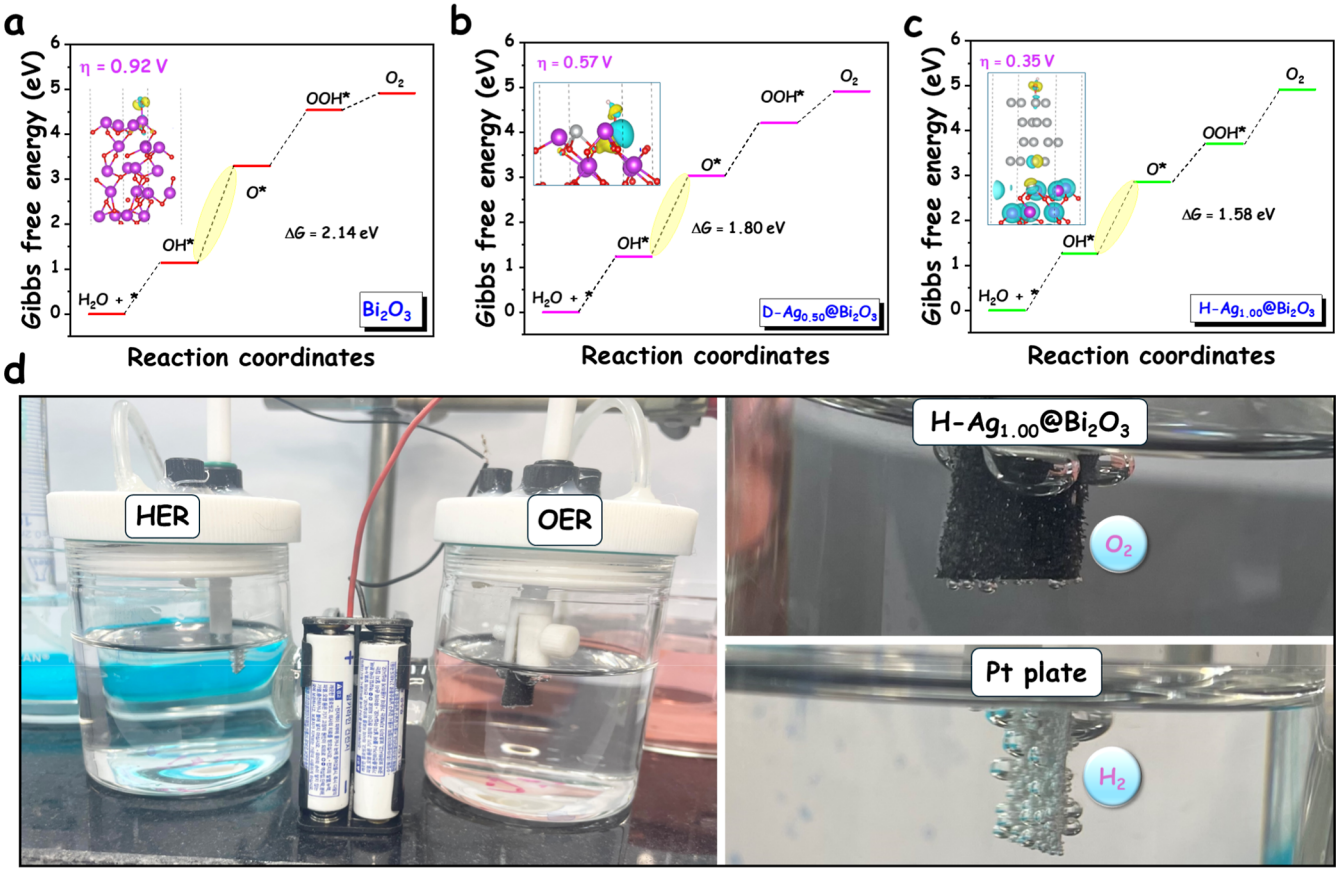

Figure 5. ΔG diagrams of (a) Bi_2O_3, (b) D-$Ag_{0.50}$@Bi_2O_3, and (c) H-$Ag_{1.00}$@Bi_2O_3 (with the inset showing the charge density difference of HO* adsorbed). (d) Full-cell test using a battery as the external supplier.

dec^{-1} and 1.3 Ω, respectively. These results indicate that the nanoplate-like structures of Bi_2O_3 create numerous nanopores, increasing the electrode/electrolyte interfaces, and the redox reaction of Bi^{2+}/Bi^{3+} contributes to the accelerated OER performance.

To investigate the effect of Ag on the OER applications, we evaluated the LSV, overpotential, Tafel slopes, and Nyquist plots for NF, pure Bi_2O_3, and Ag−Bi_2O_3 electrocatalysts with varying Ag^+ concentrations, as shown in Figure S7. Among the Ag-doped Bi_2O_3 electrodes (D-$Ag_{0.25}$@Bi_2O_3 and D-$Ag_{0.50}$@Bi_2O_3), D-$Ag_{0.50}$@Bi_2O_3 exhibited a superior performance. Similarly, among Ag−Bi_2O_3 with heterojunctions (H-$Ag_{0.75}$@Bi_2O_3, H-$Ag_{1.00}$@Bi_2O_3, H-$Ag_{1.25}$@Bi_2O_3, and H-$Ag_{1.50}$@Bi_2O_3), H-$Ag_{1.00}Bi_2O_3$ demonstrated the highest OER performance. Therefore, we compared the OER performances of D-$Ag_{0.50}$@Bi_2O_3 (doped) and H-$Ag_{1.00}$@Bi_2O_3 (heterojunction) with those of pure Bi_2O_3 and NF, as shown in Figure 4a−e. The overpotentials of D-$Ag_{0.50}$@Bi_2O_3 at 10 and 100 mA cm^{-2} were estimated to be 284 and 442 mV, respectively, with a Tafel slope of 160 mV dec^{-1} and a R_s value of 1.1 Ω. Despite containing a small amount of Ag (1.04% of Ag atomic ratio, as shown in Figure 2d), D-$Ag_{0.50}$@Bi_2O_3 achieved an impressive overpotential of less than 300 mV at 10 mA cm^{-2}. However, at higher current densities, the LSV curves of Bi_2O_3 and D-$Ag_{0.50}$@Bi_2O_3 closely overlap, indicating a lower efficiency of D-$Ag_{0.50}$@Bi_2O_3. Therefore, to transition from doping to establishing heterojunctions at the interface, we increased the Ag amount to 5.77% Ag atomic ratio (as shown in Figure 2e). As depicted in Figure 4, H-$Ag_{1.00}Bi_2O_3$ exhibits the lowest overpotentials of 260 and 406 mV at 10 and 100 mA cm^{-2}, respectively, along with the smallest Tafel slope of 141 mV dec^{-1} and an R_s value of 1 Ω. Thus, H-$Ag_{1.00}$@Bi_2O_3 represents the optimal electrocatalyst with an ideal ratio for accelerating the OER activity. H-$Ag_{1.00}$@Bi_2O_3 has been tested using the five different electrodes to clarify the highly stable OER performances (Figure S8).

Furthermore, the ECSA was determined by CV measurements across a wide range of scan rates (10−800 mV s^{-1}), as shown in Figure S9. The ECSA values increased with the Ag^+ concentration in the electrocatalysts: NF (11.62 cm^2), Bi_2O_3 (71.51 cm^2), D-$Ag_{0.50}$@Bi_2O_3 (149.57 cm^2), and H-$Ag_{1.00}$@Bi_2O_3 (178.75 cm^2). The ESCA values for the remaining samples are presented in Figure S10. The results emphasize that a higher Ag^+ concentration in the hydrothermal precursor solution leads to a larger electrochemical active area for the electrocatalysts, supported by FE-SEM analysis and OER performance data. However, despite H-$Ag_{1.50}$@Bi_2O_3 exhibiting the highest ECSA of 300.25 cm^2, its OER performance is lower than that of H-$Ag_{1.00}$@Bi_2O_3, presumably due to electrode corrosion in the 1.0 M KOH electrolyte and the presence of numerous Ag nanoparticles potentially infiltrating the pores of Bi_2O_3 and decreasing the effective surface area.

Chronopotentiometry was employed to conduct stability tests on the optimal electrocatalyst, H-$Ag_{1.00}$@Bi_2O_3. These tests were performed over various durations (25, 50, 100, and 240 h) under constant current densities of 10 mA cm^{-2} and 100 mA cm^{-2} and a high current density of 200 mA cm^{-2} in a 1.0 M KOH electrolyte, with a graphite rod used as the inert counter electrode.[34,35] As depicted in Figure S10, the stability of H-$Ag_{1.00}$@Bi_2O_3 at 10 mA cm^{-2} were 87.7% and 97.7% after

https://doi.org/10.1021/acsami.4c22156
ACS Appl. Mater. Interfaces 2025, 17, 12307−12316

25 and 50 h, respectively, but decreased to 91.1% and 77.5% after 100 and 240 h, respectively, indicating the degradation of porous morphologies (Figure 4f–h). We note that the OER stability can be manipulated by initial activation, electrode degradation, and changes in electrolyte pH.[36] The lower stability observed after 25 h (87.7%) is likely due to the inadequate adsorption of electrolyte ions onto the electrode, which may recover during subsequent electrochemical tests. Conversely, long-term stability issues may arise from complex cyclic oxidation reactions, leading to electrode degradation. Interestingly, the H-$Ag_{1.00}$@Bi_2O_3 at 100 mA cm^{-2} exhibited the most stable result of 98% compared to that of the electrode at 10 mA cm^{-2} (91.1%) and 200 mA cm^{-2} (89%) for the100 h durability test (Figure S11).

To understand the enhanced OER performance mechanism using Ag-incorporated Bi_2O_3 electrocatalysts, DFT calculations were conducted to compute the Gibbs free energy (ΔG) required for four-step OER reactions using three electrocatalysts: (i) Bi_2O_3 [Bi_2O_3 (1 1 1)], (ii) D-$Ag_{0.50}$@Bi_2O_3 [Ag(1 1 1)@Bi_2O_3 (1 1 1)], and (iii) H-$Ag_{1.00}$@Bi_2O_3 [Ag(1 1 1)@Bi_2O_3 (1 1 1) and Ag(2 2 0)@Bi_2O_3 (1 1 1)]. By estimating the spontaneous ΔG of H_2O (−12.524 eV) and H_2 (−6.59 eV) (Table S4), the extraction of "O" from H_2O results in varying ΔG values for each OER intermediate reaction step on the electrocatalyst surfaces (eqs 6–8, Table S5). Among the OER intermediate steps, the second step (HO* → O*) exhibits the highest change in the free-energy change, indicating the slowest kinetics for oxygen generation during the OER. Therefore, the efficiency of an electrocatalyst can be assessed by the extent of reduction in ΔG, specifically during this crucial second OER intermediate step. Figure 5a–c illustrates that the ΔG values for the second OER intermediate step in Bi_2O_3 [Bi_2O_3 (1 1 1)], D-$Ag_{0.50}$@Bi_2O_3 [Ag(1 1 1)@Bi_2O_3 (1 1 1)], and H-$Ag_{1.00}$@Bi_2O_3 [Ag(1 1 1)@Bi_2O_3 (1 1 1)] are 2.14, 1.80, and 1.58 eV, respectively. These values correlate with the overpotential changes (η) of these electrodes, which are 0.92, 0.57, and 0.35 V, respectively. The adsorption of HO* on the surface of each electrocatalyst, as depicted in the insets of Figure 5a–c, likely influences these results. Increasing the Ag content in the electrocatalyst accelerates the charge-transfer rate, facilitating the transfer of free electrons to the surface, thereby enhancing the adsorption of HO* and improving the OER performance.[37,38]

We also carried out DFT calculations for the H-$Ag_{1.00}$@Bi_2O_3 [Ag(2 2 0)/Bi_2O_3(1 1 1)] surfaces for H-$Ag_{1.00}$@Bi_2O_3. The catalytic activity of the H-$Ag_{1.00}$@Bi_2O_3 [Ag(2 2 0)/Bi_2O_3(1 1 1)] surfaces for the OER was found to be superior by the potential-determining step (PDS) occurring at 1.5335 V. This corresponds to an overpotential (η) of 0.3035 V, determined as the difference between the PDS potential and the equilibrium potential for the OER (1.23 V). The lower overpotential of the H-$Ag_{1.00}$@Bi_2O_3 [Ag(2 2 0)/Bi_2O_3(1 1 1)] surface indicates a more efficient catalytic performance compared to that of the H-$Ag_{1.00}$@Bi_2O_3 [Ag(1 1 1)/Bi_2O_3(1 1 1)] surface. The enhanced activity can be attributed to the higher thermodynamic stability of the Ag(2 2 0) surfaces, which facilitates favorable adsorption and activation of key intermediates involved in the OER process. These findings highlight the importance of the crystal facet in determining the catalytic efficiency of silver and underscore the role of the combination of Ag (1 1 1) and Ag(2 2 0) surfaces in H-$Ag_{1.00}$@Bi_2O_3 as a highly active site for the OER than that of D-Ag $_{0.50}$@Bi_2O_3 exhibiting only Ag (1 1 1).

To evaluate the real-time water splitting efficiency of H-$Ag_{1.00}$@Bi_2O_3 as the positive electrode, a full-cell test was conducted using external components, including two AAA batteries (1.5 V) as the power source. The negative electrode comprised a platinum plate (Pt plate) submerged in a 1.0 M KOH electrolyte. Figure 5d illustrates the generation of oxygen (O_2) on the surface of H-$Ag_{1.00}$@Bi_2O_3 and hydrogen (H_2) on the Pt plate. The total duration of water splitting was 72 h, during which corrosion was observed on the H-$Ag_{1.00}$@Bi_2O_3 electrode, as detailed in Figure S12. This study highlights the effectiveness of Ag−Bi_2O_3 heterostructures, evidenced by their lower overpotential and superior OER performance compared to previous investigations (Table 1).

Table 1. Comparison of the Overpotential at 10 mA cm^{-2} for Various Electrocatalysts in 1.0 M KOH in OER Applications

electrocatalyst	overpotential at 10 mA cm^{-2} (mV)	Tafel slope (mV dec^{-1})	refs.
Ag-doped MoO_3	344 (10 mV s^{-1})	55.0	39
$Sr_{0.9}Ag_{0.1}RuO_3$	220	156.0	40
NiCo@Ag_{40}/Nf-Ar	370 (140 mA cm^{-2})	104.0	41
Ag-doped CoOOH	256	64.6	42
Ag/NiFe LDH	267	23	43
$Ag_{0.2}Ni_{0.8}O$	305	93	44
AV-Er_2O_3-doped δ-Bi_2O_3	445		45
Ag_3PO_4−Bi_2WO_6−TiO_2	360	64	46
[Ag + Bi]O_x	700 (100 mA cm^{-2})	70	47
H-Ag1.00@Bi2O3	260	141	this work

EXPERIMENTAL SECTION

Materials. Ag nitrate (ACS reagent, ≥99.0%), bismuth(III)nitrate pentahydrate (ACS reagent, ≥98.0%), potassium hydroxide (ACS reagent, ≥85.0%, pellets), and sulfuric acid (ACS reagent, 95.0%–98.0%) were sourced from Sigma-Aldrich (Germany). Solvents, including DI water and acetone, were obtained from Samchun (Korea).

Preparation of Ag−Bi_2O_3 Electrocatalysts. A piece of nickel foam (2 × 4 cm) was sanitized with sulfuric acid, DI water, and acetone. The detailed process was reported in our previous publication.[48] The cleaned nickel foam was placed in a Teflon liner, and 60 mL of a 5 mM $Bi(NO_3)_3$ solution was added. Various concentrations of Ag, ranging from 0 mM (Bi_2O_3), 0.25 mM (D-$Ag_{0.25}$@Bi_2O_3), 0.50 mM (D-$Ag_{0.50}$@Bi_2O_3), 0.75 mM (H-$Ag_{0.75}$@Bi_2O_3), 1.00 mM (H-$Ag_{1.00}$@Bi_2O_3), and 1.25 mM (H-$Ag_{1.25}$@Bi_2O_3) to 1.50 mM (H-$Ag_{1.50}$@Bi_2O_3), were incorporated into Bi_2O_3 to form the composites. The hydrothermal reactions were maintained at 180 °C for 6 h. Afterward, the samples were rinsed with DI water and acetone and dried at room temperature (Scheme 1). The details of the synthesis conditions are described in Table S1.

CONCLUSIONS

In this work, we synthesized a bismuth-oxide (Bi_2O_3) electrocatalyst incorporated with silver (Ag) elements by a facile one-step hydrothermal method for application in OER. We studied morphologies and electrochemical behavior of the doped- and heterojunction-formed Ag−Bi_2O_3 electrodes manipulated by the various concentrations of Ag NPs in the hydrothermal precursor solutions. According to the results, we explored each role of Ag, Bi_2O_3, and Ag−Bi_2O_3 composites:

https://doi.org/10.1021/acsami.4c22156
ACS Appl. Mater. Interfaces 2025, 17, 12307−12316

Scheme 1. Schematics Showing the Synthesis of Ag−Bi_2O_3 Electrocatalysts

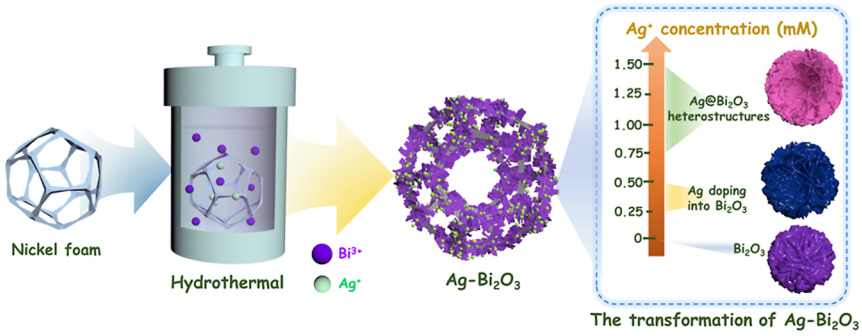

(1) a large surface area of the Ag electrode created by Bi_2O_3 nanoplate morphologies can accelerate the OER activity due to the increased electrode/electrolyte interfaces; (2) the excellent conductivity of Ag NPs and the low band gap of Bi_2O_3 semiconductor can allow the high rate of electron transfer, resulting in the rapid OER; and (3) the interaction of Ag−Bi in the bimetallic can improve the conductivity and simultaneously increase the active sites as well as the stability compared to that of the individual materials. The optimized electrode (H-$Ag_{1.00}$@Bi_2O_3), synthesized with 1.0 mM Ag in the hydrothermal precursor solution, exhibited superior OER performance, achieving a low overpotential of 260 mV at a current density of 10 mA cm^{-2} in the 1.0 M KOH electrolyte, a corresponding Tafel slope of 141 mV dec^{-1}, and a low impedance of 1.0 Ω. Furthermore, the durability of the electrodes was demonstrated by stability values of Ag@Bi_2O_3 after testing for 100 (91.1%) and 240 h (77.5%). The performances in a full-cell test using double AAA batteries further demonstrated the robust properties of the electrocatalyst. Theoretical DFT calculations supported the experimental findings by providing ΔG values for each intermediate reaction of the OER. This approach to create the noble metal-decorated post-transition metal composite electrocatalyst would be further utilized to explore other effective combinations of electrocatalysts for accelerating the OER reaction.

■ ASSOCIATED CONTENT

Supporting Information

The Supporting Information is available free of charge at https://pubs.acs.org/doi/10.1021/acsami.4c22156.

XRD patterns of pure Ag and Bi_2O_3 electrodes illustration showing the XRD measurement; SAED analysis of D-$Ag_{0.50}$@Bi_2O_3 and H-$Ag_{1.00}$@Bi_2O_3; FE-SEM image of H-$Ag_{1.50}$@Bi_2O_3; EDS-mapping of D-$Ag_{0.50}$@Bi_2O_3 and H-$Ag_{1.00}$@Bi_2O_3 characterized by HR-TEM; XPS spectrum and high-resolution XPS survey of Bi_2O_3, Bi 4f, and O 1s; LSV with iR correction curves of OER overpotential (η) at the current densities of 10 and 100 mA cm^{-2}, corresponding Tafel plots, and Nyquist plots of the various Ag−Bi_2O_3 electrodes; compared LSV curves of five H-$Ag_{1.00}$@Bi_2O_3; CV and C_{dl} results of the various Ag−Bi_2O_3 electrodes at different scan rates (10−200 mV s^{-1}); ECSA values of the various Ag−Bi_2O_3 electrodes (denoted I−D-$Ag_{0.25}$@Bi_2O_3, II−D-$Ag_{0.50}$@Bi_2O_3, III−H−$Ag_{0.75}$@Bi_2O_3, IV−H-$Ag_{1.00}$@Bi_2O_3, V−H-$Ag_{1.25}$@Bi_2O_3, and VI−H-$Ag_{1.50}$@Bi_2O_3); chronopotentiometry test for 25 h, 50 h, 240 h, and stability results of H-$Ag_{1.00}$@Bi_2O_3 for various durations; chronopotentiometry test of H-$Ag_{1.00}$@Bi_2O_3 for 100 h at different current densities of 100 mA cm^{-2} and 200 mA cm^{-2}; photos showing the experimental setup for the full cell test and electrolyte before and after the stability test for 72 h ; synthetic conditions for electrocatalysts; comparison between the atomic ratios (%) of Bi 4f and Ag 3d extracted from XPS results and molar ratios of Bi^{3+} and Ag^{+} used in experiments for synthesizing the D-$Ag_{0.50}$@Bi_2O_3 and H-$Ag_{1.00}$@Bi_2O_3, respectively; comparison between the ICP-OES results and the molar ratio of hydrothermal precursor solution for D-$Ag_{0.50}$@Bi_2O_3 and H-$Ag_{1.00}$@Bi_2O_3; free energy of H_2O and H_2 calculated; and ΔG of Bi_2O_3, D-$Ag_{0.50}$@Bi_2O_3, and H-$Ag_{1.00}$@Bi_2O_3 calculation (PDF)

■ AUTHOR INFORMATION

Corresponding Authors

Umesh T. Nakate − *Department of Nano Convergence Engineering, Department of Polymer-Nano Science and Technology, Jeonbuk National University, Jeonju 54896, Republic of Korea; Department of Chemical Engineering, Hanyang University, Seoul 04763, Republic of Korea;* orcid.org/0000-0001-8268-0385; Email: umesh.nakate@gmail.com

Sungjune Park − *School of Chemical Engineering, Sungkyunkwan University, Suwon 16419, Republic of Korea;* orcid.org/0000-0003-0237-0083; Email: sungjunepark@skku.edu

Authors

Que Thi Nguyen − *School of Chemical Engineering, Sungkyunkwan University, Suwon 16419, Republic of Korea*

Balaji G. Ghule − *School of Energy and Chemical Engineering, Ulsan National Institute of Science and Technology, Ulsan 44919, Republic of Korea*

Soojin Park − *Department of Nano Convergence Engineering, Department of Polymer-Nano Science and Technology, Jeonbuk National University, Jeonju 54896, Republic of Korea*

Jeongsik Choi − *Department of Nano Convergence Engineering, Department of Polymer-Nano Science and Technology, Jeonbuk National University, Jeonju 54896, Republic of Korea*

Jong Hyun Park − *Materials Science and Chemical Engineering Center, Institute for Advanced Engineering, Yongin 17180, Republic of Korea*

Jae Ryang Park − *Materials Science and Chemical Engineering Center, Institute for Advanced Engineering, Yongin 17180, Republic of Korea*

Ji-Hyun Jang − *School of Energy and Chemical Engineering, Ulsan National Institute of Science and Technology, Ulsan 44919, Republic of Korea;* orcid.org/0000-0003-4364-6605

Dong-Won Kim − *Department of Chemical Engineering, Hanyang University, Seoul 04763, Republic of Korea;* orcid.org/0000-0002-1735-0272

Complete contact information is available at: https://pubs.acs.org/10.1021/acsami.4c22156

Author Contributions

The manuscript was written through contributions of all authors. All authors have given approval to the final version of the manuscript.

Notes

The authors declare no competing financial interest.

■ ACKNOWLEDGMENTS

This work was supported by the National Research Foundation of Korea (NRF) grant funded by the Korean government (MSIT) (RS-2024-00335216).

■ REFERENCES

(1) Tee, S. Y.; Win, K. Y.; Teo, W. S.; Koh, L.; Liu, S.; Teng, C. P.; Han, M. Recent Progress in Energy-Driven Water Splitting. *Adv. Sci.* **2017**, *4* (5), 1600337.

(2) Sazali, N. Emerging Technologies by Hydrogen: A Review. *Int. J. Hydrogen Energy* **2020**, *45* (38), 18753−18771.

(3) Liu, Y.; Zhou, D.; Deng, T.; He, G.; Chen, A.; Sun, X.; Yang, Y.; Miao, P. Research Progress of Oxygen Evolution Reaction Catalysts for Electrochemical Water Splitting. *ChemSusChem* **2021**, *14* (24), 5359−5383.

(4) Wu, A.; Xie, Y.; Ma, H.; Tian, C.; Gu, Y.; Yan, H.; Zhang, X.; Yang, G.; Fu, H. Integrating the Active OER and HER Components as the Heterostructures for the Efficient Overall Water Splitting. *Nano Energy* **2018**, *44*, 353−363.

(5) Zhou, Y.-N.; Yu, W.-L.; Cao, Y.-N.; Zhao, J.; Dong, B.; Ma, Y.; Wang, F.-L.; Fan, R.-Y.; Zhou, Y.-L.; Chai, Y.-M. S-Doped Nickel-Iron Hydroxides Synthesized by Room-Temperature Electrochemical Activation for Efficient Oxygen Evolution. *Appl. Catal. B Environ.* **2021**, *292*, 120150.

(6) Reier, T.; Oezaslan, M.; Strasser, P. Electrocatalytic Oxygen Evolution Reaction (OER) on Ru, Ir, and Pt Catalysts: A Comparative Study of Nanoparticles and Bulk Materials. *ACS Catal.* **2012**, *2* (8), 1765−1772.

(7) Tsai, F.-T.; Deng, Y.-T.; Pao, C.-W.; Chen, J.-L.; Lee, J.-F.; Lai, K.-T.; Liaw, W.-F. The HER/OER Mechanistic Study of an FeCoNi-Based Electrocatalyst for Alkaline Water Splitting. *J. Mater. Chem. A* **2020**, *8* (19), 9939−9950.

(8) Cui, Y.; Xue, Y.; Zhang, R.; Zhang, J.; Li, X.; Zhu, X. Vanadium−Cobalt Oxyhydroxide Shows Ultralow Overpotential for the Oxygen Evolution Reaction. *J. Mater. Chem. A* **2019**, *7* (38), 21911−21917.

(9) Bhanja, P.; Mohanty, B.; Patra, A. K.; Ghosh, S.; Jena, B. K.; Bhaumik, A. IrO_2 and Pt Doped Mesoporous SnO_2 Nanospheres as Efficient Electrocatalysts for the Facile OER and HER. *ChemCatChem* **2019**, *11* (1), 583−592.

(10) Rongan, H.; Haijuan, L.; Huimin, L.; Difa, X.; Liuyang, Z. S-Scheme Photocatalyst Bi_2O_3/TiO_2 Nanofiber with Improved Photocatalytic Performance. *J. Mater. Sci. Technol.* **2020**, *52*, 145−151.

(11) Khan, A. ur R.; Ramzan, M.; Alanazi, S. J. F.; Al-Mohaimeed, A. M.; Ali, S.; Imran, M.; Majid, M. A.; Sarfraz, M. H. Structural, Optical, Electrical and Photocatalytic Investigation of n-Type Zn^{2+}-Doped α-Bi_2O_3 Nanoparticles for Optoelectronics Applications. *ACS Omega* **2024**, *9* (21), 22650−22659.

(12) Mandawade, A. S.; Sonawane, L. D.; Ahemad, H. I.; Aher, Y. B.; Gite, A. B.; Nikam, L. K.; Jain, G. H.; Femi, M. D.; Patil, G. E.; Palve, B. M.; Shinde, M. S. Gas Sensing and Photocatalytic Activity of Synthesized Hierarchical Bi_2O_3 Nanoflakes by Sol−Gel and Nanosheets by Hydrothermal Method. *J. Mater. Sci. Mater. Electron.* **2024**, *35* (14), 989.

(13) Ma, Y.; Bai, Y.; Liang, B.; Yang, R.; Zheng, S.; Hu, C.; Zhang, C.; Qin, F.; Wei, L. MOF-Derived Hierarchical Bi_2O_3 as Advanced Anode for Ni/Bi Alkaline Battery with High Energy Density. *Colloids Surf., A* **2022**, *633*, 127896.

(14) Guo, H.; Yin, H.; Yan, X.; Shi, S.; Yu, Q.; Cao, Z.; Li, J. Pt-Bi Decorated Nanoporous Gold for High Performance Direct Glucose Fuel Cell. *Sci. Rep.* **2016**, *6*, 39162.

(15) Dey, S.; Mandal, M. K.; Pramanik, S.; Atta, S.; Basu, S. Bi_2O_3-Incorporated Carbon-Supported Bismuth-Silver (Bi@Ag/C) Nanoparticle as an Efficient and Stable Electrocatalyst for Glucose Electro-Oxidation. *Ionics* **2023**, *29* (3), 1101−1113.

(16) Subin David, S. P.; Veeralakshmi, S.; Sandhya, J.; Nehru, S.; Kalaiselvam, S. Room Temperature Operatable High Sensitive Toluene Gas Sensor Using Chemiresistive Ag/Bi_2O_3 Nanocomposite. *Sensors Actuators B Chem.* **2020**, *320*, 128410.

(17) Wang, X.; He, W.; Shi, J.; Junqueira, J. R. C.; Zhang, J.; Dieckhöfer, S.; Seisel, S.; Das, D.; Schuhmann, W. Ag-induced Phase Transition of Bi_2O_3 Nanofibers for Enhanced Energy Conversion Efficiency towards Formate in CO_2 Electroreduction. *Chem.—Asian J.* **2023**, *18* (2), No. e202201165.

(18) Zhao, S.; Yang, Y.; Lu, R.; Wang, Y.; Lu, Y.; Rodriguez, R. D.; Sheremet, E.; Chen, J. Enhanced Selective Adsorption and Photocatalytic of Ag/Bi_2O_3 Heterostructures Modified up-Conversion Nanoparticles. *J. Environ. Chem. Eng.* **2022**, *10* (1), 107107.

(19) Du, X.; Guo, J.; Chen, M.; Cheong, W.-C.; Chen, Y.; Liu, D.; Chen, S.; Wang, X.; Ho Lo, K.; Hu, J.-S.; Pan, H. Surface Reconstruction on Silver Nanoparticles Decorated Trimetallic Hydroxide Nanosheets to Generate Highly Active Oxygen-Deficient (Oxy)Hydroxide Layer for High-Efficient Water Oxidation. *Chem. Eng. J.* **2021**, *425*, 131662.

(20) Kim, M.; Park, J.; Kang, M.; Kim, J. Y.; Lee, S. W. Toward Efficient Electrocatalytic Oxygen Evolution: Emerging Opportunities with Metallic Pyrochlore Oxides for Electrocatalysts and Conductive Supports. *ACS Cent. Sci.* **2020**, *6* (6), 880−891.

(21) Ede, S. R.; Luo, Z. Tuning the Intrinsic Catalytic Activities of Oxygen-Evolution Catalysts by Doping: A Comprehensive Review. *J. Mater. Chem. A* **2021**, *9* (36), 20131−20163.

(22) Li, Y.; Tang, G.; Wang, Y.; Chai, Y.; Liu, C. Interfacial Engineering of a Phase-Controlled Heterojunction for High-Efficiency HER, OER, and ORR Trifunctional Electrocatalysis. *ACS Omega* **2022**, *7* (16), 13687−13696.

(23) Wang, N.; Li, X.; Yang, Y.; Zhou, Z.; Shang, Y.; Zhuang, X.; Zhang, T. Two-Stage Calcination Composite of Bi_2O_3-TiO_2 Supported on Powdered Activated Carbon for Enhanced Degradation of Sulfamethazine under Solar Irradiation. *J. Water Process Eng.* **2020**, *35*, 101220.

(24) Shi, J.; Xie, Z.; Tang, X.; Wang, Y.; Yuan, G.; Liu, J.-M. Enhanced Piezo-Photocatalytic Performance of $Ag@Na_{0.5}Bi_{0.5}TiO_3$ Composites. *J. Alloys Compd.* **2022**, *911*, 164885.

(25) Gu, C.; Zhang, Z.; Zhao, F.; Zhang, Y.; Liu, Y.; Sun, Q. Preparation of Ultrafine Ag_3BiO_3 and Modification Mechanism on EMD Cathode for Rechargeable Alkaline Manganese Dioxide Battery. *J. Mater. Sci. Mater. Electron.* **2023**, *34* (23), 1667.

(26) Liu, B.; Yasin, A. S.; Musho, T.; Bright, J.; Tang, H.; Huang, L.; Wu, N. Visible-Light Bismuth Iron Molybdate Photocatalyst for Artificial Nitrogen Fixation. *J. Electrochem. Soc.* **2019**, *166* (5), H3091−H3096.

(27) Nguyen, Q. T.; Nakate, U. T.; Chen, J.; Wei, Y.; Park, S. High-Performance Oxygen Evolution Reaction Activity at Low and Higher Current Densities Using Nanostructured CeO_2 and Plasma-Assisted $Bi@CeO_2$ Electrocatalysts. *Mater. Sci. Eng., B* **2022**, *286*, 116014.

(28) Gerber, S. J.; Erasmus, E. Electronic Effects of Metal Hexacyanoferrates: An XPS and FTIR Study. *Mater. Chem. Phys.* **2018**, *203*, 73−81.

(29) Quintana-Solórzano, R.; Mejía-Centeno, I.; Armendáriz-Herrera, H.; Ramírez-Salgado, J.; Rodríguez-Hernandez, A.; Guzmán-Castillo, M. de L.; Lopez Nieto, J. M.; Valente, J. S. Discerning the Metal Doping Effect on Surface Redox and Acidic Properties in a MoVTeNbO$_x$ for Propa(e)Ne Oxidation. *ACS Omega* **2021**, *6* (23), 15279−15291.
(30) Vidyasagar, D.; Ghugal, S. G.; Kulkarni, A.; Mishra, P.; Shende, A. G.; Jagannath; Umare, S. S.; Sasikala, R. Silver/Silver(II) Oxide (Ag/AgO) Loaded Graphitic Carbon Nitride Microspheres: An Effective Visible Light Active Photocatalyst for Degradation of Acidic Dyes and Bacterial Inactivation. *Appl. Catal. B Environ.* **2018**, *221*, 339−348.
(31) Wang, D.; Yu, X.; Feng, Q.; Lin, X.; Huang, Y.; Huang, X.; Li, X.; Chen, K.; Zhao, B.; Zhang, Z. In-Situ Growth of β-Bi$_2$O$_3$ Nanosheets on g-C$_3$N$_4$ to Construct Direct Z-Scheme Heterojunction with Enhanced Photocatalytic Activities. *J. Alloys Compd.* **2021**, *859*, 157795.
(32) Han, X.; Li, Y.; Wang, H.; Zhang, Q. Controlled Preparation of β-Bi$_2$O$_3$/Mg−Al Mixed Metal Oxides Composites with Enhanced Visible Light Photocatalytic Performance. *Res. Chem. Intermed.* **2020**, *46* (11), 5009−5021.
(33) Hu, X.; Tian, X.; Lin, Y.-W.; Wang, Z. Nickel Foam and Stainless Steel Mesh as Electrocatalysts for Hydrogen Evolution Reaction, Oxygen Evolution Reaction and Overall Water Splitting in Alkaline Media. *RSC Adv.* **2019**, *9* (54), 31563−31571.
(34) Zhou, Y.-N.; Li, F.-T.; Dong, B.; Chai, Y.-M. Double Self-Reinforced Coordination Modulation Constructing Stable Ni^{4+} for Water Oxidation. *Energy Environ. Sci.* **2024**, *17* (4), 1468−1481.
(35) Park, S.; Nguyen, Q. T.; Choi, J.; Park, J. H.; Park, J. R.; Nakate, U. T.; Park, S. Au-Nanoparticles-Decorated CeO$_2$ Electrocatalyst Synthesized by Direct Growth and Wet Impregnation for Enhanced Oxygen Evolution Reaction. *Surf. Interfaces* **2023**, *41*, 103206.
(36) Zeng, F.; Mebrahtu, C.; Liao, L.; Beine, A. K.; Palkovits, R. Stability and Deactivation of OER Electrocatalysts: A Review. *J. Energy Chem.* **2022**, *69*, 301−329.
(37) Mao, L.; Huang, Y.; Deng, H.; Meng, F.; Fu, Y.; Wang, Y.; Li, M.; Zhang, Q.; Dong, C.; Gu, L.; Shen, S. Synergy of Ultrathin CoO$_x$ Overlayer and Nickel Single Atoms on Hematite Nanorods for Efficient Photo-Electrochemical Water Splitting. *Small* **2023**, *19* (7), 2203838.
(38) Yoon, K. Y.; Park, J.; Jung, M.; Ji, S. G.; Lee, H.; Seo, J. H.; Kwak, M. J.; Il Seok, S.; Lee, J. H.; Jang, J. H. NiFeO$_x$ Decorated Ge-Hematite/Perovskite for an Efficient Water Splitting System. *Nat. Commun.* **2021**, *12*, 4309.
(39) Jansi Rani, B.; Ravi, G.; Yuvakkumar, R.; Ameen, F.; AlNadhari, S.; Hong, S. I. Fabrication and Electrochemical OER Activity of Ag Doped MoO$_3$ Nanorods. *Mater. Sci. Semicond. Process.* **2020**, *107* (2), 104818.
(40) Wang, Y.; Wu, J.; Lu, X.; Guo, Y.; Zhao, H.; Tang, X. A-Site Doped Ruthenium Perovskite Bifunctional Electrocatalysts with High OER and ORR Activity. *J. Alloys Compd.* **2022**, *920* (November 2018), 165770.
(41) Yan, K.-L.; Chi, J.-Q.; Liu, Z.-Z.; Dong, B.; Lu, S.-S.; Shang, X.; Gao, W.-K.; Chai, Y.-M.; Liu, C.-G. Coupling Ag-Doping and Rich Oxygen Vacancies in Mesoporous NiCoO Nanorods Supported on Nickel Foam for Highly Efficient Oxygen Evolution. *Inorg. Chem. Front.* **2017**, *4* (11), 1783−1790.
(42) Lee, C.; Shin, K.; Jung, C.; Choi, P.-P.; Henkelman, G.; Lee, H. M. Atomically Embedded Ag via Electrodiffusion Boosts Oxygen Evolution of CoOOH Nanosheet Arrays. *ACS Catal.* **2020**, *10* (1), 562−569.
(43) Liu, S.; Ren, S.; Gao, R.-T.; Liu, X.; Wang, L. Atomically Embedded Ag on Transition Metal Hydroxides Triggers the Lattice Oxygen towards Sustained Seawater Electrolysis. *Nano Energy* **2022**, *98* (July 2022), 107212.
(44) Iqbal, M. Z.; Kriek, R. J. Silver/Nickel Oxide (Ag/NiO) Nanocomposites Produced Via a Citrate Sol-Gel Route as Electrocatalyst for the Oxygen Evolution Reaction (OER) in Alkaline Medium. *Electrocatalysis* **2018**, *9* (3), 279−286.
(45) Azhar, S.; Ahmad, K. S.; Abrahams, I.; Jaffri, S. B.; Ingsel, T.; Gupta, R. K.; Ali, D. Biomimetic [AV-Er$_2$O$_3$-Doped δ-Bi$_2$O$_3$]-Stacked Nanoplates: An Efficient Electrocatalyst for OER/HER and Electrode Material for Supercapacitor Application. *Ionics* **2023**, *29* (6), 2485−2500.
(46) Mandari, K. K.; Son, N.; Kang, M. Ag$_3$PO$_4$-Bi$_2$WO$_6$-TiO$_2$ as a High Performance Electrocatalyst for Oxygen Evolution Reaction. *Appl. Surf. Sci.* **2021**, *566* (July), 150681.
(47) Simondson, D.; Chatti, M.; Gardiner, J. L.; Kerr, B. V.; Hoogeveen, D. A.; Cherepanov, P. V.; Kuschnerus, I. C.; Nguyen, T. D.; Johannessen, B.; Chang, S. L. Y.; MacFarlane, D. R.; Hocking, R. K.; Simonov, A. N. Mixed Silver−Bismuth Oxides: A Robust Oxygen Evolution Catalyst Operating at Low PH and Elevated Temperatures. *ACS Catal.* **2022**, *12* (20), 12912−12926.
(48) Nguyen, Q. T.; Nakate, U. T.; Chen, J.; Tran, D. T.; Park, S. Hybrid Nanostructured Bismuth-cobalt Oxides/Hydroxides Binder-free Electrodes Fabricated by Two-step Electrodeposition for High-performance Supercapacitors. *Int. J. Energy Res.* **2022**, *46* (9), 12254−12265.

https://doi.org/10.1021/acsami.4c22156
ACS Appl. Mater. Interfaces 2025, 17, 12307−12316